

Disentangling $\gamma - \beta$: the 4th-order velocity moments based on spherical Jeans analysis

M. Dafa Wardana,¹ Masashi Chiba,¹ and Kohei Hayashi^{2,1,3}

¹*Astronomical Institute, Tohoku University, 6-3 Aoba, Sendai, Japan*

²*National Institute of Technology, Sendai College, 48 Nodayama, Natori, Japan*

³*ICRR, The University of Tokyo, 5-1-5 Kashiwanoha, Kashiwa, Japan*

ABSTRACT

Distinguishing a core and a cusp within dark matter halos is complexified by the existence of mass-anisotropy degeneracy, where various combinations of velocity anisotropy (β) and inner density slope (γ) yield similar observational signatures. We construct a dynamical model that incorporates the 4th-order velocity moments to alleviate this challenge. The inclusion of the 4th-order velocity moments enables stars' line-of-sight velocity distribution (LOSVD) to be flexible. This flexible LOSVD can cover from a thin-tailed to a heavy-tailed distribution that is inaccessible if only the 2nd-order moments are considered. We test our dynamical model using mock galaxies and find that a ratio of the global line-of-sight velocity dispersion of the mock galaxy to the velocity error measurement $\sigma_{\text{los,global}}/\Delta v_{\text{los}} \gtrsim 4$ is required to avoid obtaining systematically biased results. This bias arises from the strong dependency of the 4th-order moments on the LOSVD tails, and not even increasing the sample size to 10^4 stars can mitigate its effect. In that velocity ratio, β is recovered within $\sim 1\sigma$ even when the sample size is only 500 stars, regardless of the recovery of the other parameters. However, the estimation of γ varies, depending on the degree to which LOSVDs deviate from Gaussianity. Because of the more significant change in its LOSVDs, a cored dark halo is more likely to be identified than a cusp.

Unified Astronomy Thesaurus concepts: Dark matter (353) — Dwarf spheroidal galaxy (420) — Stellar kinematics (1608)

1. INTRODUCTION

The Λ CDM theory has been facing some challenges, specifically in the subgalactic scales, with the core-cusp problem (Flores & Primack 1994; Moore 1994; Burkert 1995) being one of the oldest (see Bullock & Boylan-Kolchin (2017) for a review). This problem signifies a discrepancy in the central density slope of dark matter halos as inferred from simulations involving only dark matter particles compared to those inferred from the analysis of observational data. Dark matter-only simulations predict the universality of the dark matter density profile that rises steeply in the inner part following $\rho(r) \propto r^{-\gamma}$, with $\gamma \approx 1.0$ regardless the initial condition, well known as the NFW profile (Navarro et al. 1996). This universal property is in tension with the results from kinematics analyses using observational data from various types of dwarf galaxies that do not converge and instead favor a diverse inner density slope where $0 \lesssim \gamma \lesssim 1.5$ (e.g., Oh et al. (2015)).

While the existence of the core profile remains a subject of debate and is potentially constrained by modeling limitations (de Blok 2010), the focus of probing a dark matter density profile has been redirected from gas-rich dwarf spirals to the nearby region; satellites of the Milky Way. The Milky Way dwarf spheroidal (dSph) and ultra-faint dwarf (UFD) satellites are among the most dark matter-dominated as well as the oldest gravitational systems known at the moment (Simon 2019; Battaglia & Nipoti 2022). These types of galaxies are believed to be the building blocks of the MW-sized galaxies and retain the most pristine relics of ancient structures from the early universe. Their unbeatable low fraction of baryon content, even inside the half-light radius, makes them the most attractive sites to test dark matter theories because the baryonic effects are less significant compared to galaxies with a higher fraction of baryonic

component. Their proximity also offers a key advantage that enables their member stars to be resolved, allowing for the line-of-sight velocity, projected position, and metallicity of the member stars to be obtained individually.

Modeling the internal dynamics of dSphs and UFDs has been considered one of the primary pathways in addressing the core-cusp problem (see [Battaglia et al. \(2013\)](#) for a review). Despite the advantages mentioned earlier, distinguishing between a core and a cusp remains challenging. Obtained results are often unable to robustly discriminate the two profiles from each other based on the available data set ([Breddels et al. 2013](#); [Geringer-Sameth et al. 2015](#)). One central problem is the mass-anisotropy degeneracy, i.e., effects due to only three phase spaces (the position on the sky plane and line-of-sight velocity) that are observable. Consequently, there exists a broad range of models with velocity anisotropies and density profiles consistent with observations. Improvements from various directions are made to break this degeneracy.

Where available, the use of more than one chemodynamically distinct stellar population can partially alleviate the degeneracy ([Walker & Peñarrubia 2011](#); [Amorisco & Evans 2012](#); [Kowalczyk & Lokas 2022](#)). Motivated by the elongated observed stellar distribution and non-sphericity of simulated dark halo, there are also attempts to explore axisymmetric models, investigating different kinematical signatures along the major and minor axes ([Hayashi & Chiba 2012, 2015](#); [Hayashi et al. 2020](#)). Other groups aim to mitigate this degeneracy by developing Schwarzschild orbital-based superposition methods, assuming either a spherically symmetric ([Breddels et al. 2013](#); [Kowalczyk et al. 2019](#)) or axisymmetric ([Jardel & Gebhardt 2012](#); [Jardel et al. 2013](#); [Hagen et al. 2019](#)) underlying gravitational potential. Another approach involves utilizing higher-order moments through the virial shape parameter ([Richardson & Fairbairn 2014](#); [Genina et al. 2020](#)) or Jeans modeling ([Lokas 2002, 2009](#); [Richardson & Fairbairn 2013](#)).

The limited exploration through the higher-order moments primarily stems from their heavy reliance on stars in the velocity tails and large sample size requirements ([Merrifield & Kent 1990](#)). The analysis involving higher-order moments is further complicated by the substantial impact of interlopers, which can significantly alter the velocity distribution in the tails where the star count is low. Nevertheless, this situation is going to be improved in the near future, thanks to the Subaru Prime Focus Spectrograph project that will increase the kinematic sample in each of the targeted MW's dwarf galaxies to approximately 5,000 stars with expected velocity error measurement of $\sim 2 \text{ km s}^{-1}$ ([Takada et al. 2014](#); [Tamura et al. 2016](#); [Hayashi et al. 2023a](#)). Therefore, exploring the ability and behavior of the higher-order moments to mitigate mass-anisotropy degeneracy becomes a subject of investigation. In this work, we construct a dynamical model based on the spherically symmetric 2nd-order combined with 4th-order Jeans equations.

This paper is organized as follows. We initiate by detailing the dynamical model, which relies on the spherically symmetric 2nd-order and 4th-order Jeans equations, in Section 2. Section 3 presents the outcomes derived from applying the model to mock data. In section 4, we discuss the dependency on the choice of prior, the recovery of γ , and the recovery of β . We summarize our main conclusions in section 5.

2. MODELS

This section consists of an explanation of the dark matter and star distribution we adopt (Section 2.1), the 2nd-order (Section 2.2) and 4th-order (Section 2.3) Jeans modeling that we apply, the fitting procedure to marginalize parameters (Section 2.4), and details of the mock data (Section 2.5).

Due to the dark matter domination even in the inner part of the galaxy, we assume that stars only act as tracers inside a gravitational potential provided by dark matter. We also assume that the effects of binaries are removed from the l.o.s. velocity dispersion and kurtosis profile and consider the case of a perfect determination of stars' membership.

2.1. Dark matter density and light profiles

For the dark matter density profile, we adopt the Generalized Hernquist model introduced by [Hernquist \(1990\)](#) and [Zhao \(1996\)](#)

$$\rho_{\text{dm}}(r) = \rho_0 \left(\frac{r}{a_{\text{dm}}} \right)^{-\gamma} \left[1 + \left(\frac{r}{a_{\text{dm}}} \right)^{\beta_{\text{trans}}} \right]^{-(\alpha-\gamma)/\beta_{\text{trans}}}. \quad (1)$$

In Equation (1), ρ_0 is the dark matter scale density, a_{dm} is the dark matter scale length, γ is the inner density slope, β_{trans} is the transition sharpness between the inner and the outer slope density profile. A smaller value of β_{trans} means a smoother, more gradual change from the inner slope to the outer slope. The last parameter, α , is the outer slope density profile that dominates the slope of the density profile in the galactocentric distance larger than a_{dm} . This model provides a wide range of density profiles, including the cored profile ($\gamma \approx 0$), the cuspy profile ($\gamma \approx 1$), and any possible profiles between the two.

For the light profile, we adopt the Plummer model (Plummer 1911) that is given by

$$\nu(r) = \frac{3L}{4\pi a_*^3} \left(1 + \frac{r^2}{a_*^2}\right)^{-5/2}, \quad (2)$$

where $\nu(r)$ is the 3-dimension light profile, L is the total luminosity of the stellar system, and a_* is a Plummer scale length, which in this case, also corresponds to the projected half-light radius. The observable projected light profile $I(R)$, where R is the projected radius on the sky plane, can be obtained by integrating along the line-of-sight, which results

$$I(R) = \frac{L}{\pi a_*^2} \left(1 + \frac{R^2}{a_*^2}\right)^{-2}. \quad (3)$$

For simplicity, we introduce a dimensionless parameter $b \equiv a_{\text{dm}}/a_*$.

2.2. Spherically symmetric 2nd-order Jeans equations

Assuming that a gravitational system is static and spherical, the motion of its stars moving under the influence of underlying gravitational potential $\Phi(r)$ can be explained by the distribution function $f(\mathbf{r}, \mathbf{v})$. However, the distribution function is inaccessible in the real application. Jeans equations link the inaccessible distribution function to the gravitational potential via velocity moments. Defining velocity moments with spherical coordinates (r, θ, ϕ) as

$$\overline{\nu v_r^i v_\theta^j v_\phi^k} = \int d^3v v_r^i v_\theta^j v_\phi^k f. \quad (4)$$

For the second order, velocity moments represent the velocity dispersions $\overline{v_r^2} = \sigma_r^2$, $\overline{v_\theta^2} = \sigma_\theta^2$, and $\overline{v_\phi^2} = \sigma_\phi^2$, where the streaming motions are assumed to be zero. The 2nd-order Jeans equations can be written as (Binney & Tremaine 2008)

$$\frac{d}{dr} \nu \sigma_r^2 + 2 \frac{\beta}{r} \nu \sigma_r^2 + \nu \frac{d\Phi}{dr} = 0, \quad (5)$$

where the velocity anisotropy β is defined as $\beta \equiv 1 - (\sigma_\theta^2 + \sigma_\phi^2)/2\sigma_r^2$. In the case of constant β , i.e., assuming the distribution function is in the form of $f(E, L) = f_0(E)L^{-2\beta}$, where E and L denote the total energy and angular momentum, respectively, the solution of Equation (5) that satisfies the boundary condition $\lim_{r \rightarrow \infty} \sigma_r^2 = 0$ is

$$\sigma_r^2(r) = \frac{1}{r^{2\beta} \nu(r)} \int_r^\infty dr' r'^{2\beta} \nu(r') \frac{d\Phi}{dr'}, \quad (6)$$

The observable line-of-sight velocity dispersion σ_{los} as a function of projected radius, R , can be obtained by integrating along the line-of-sight

$$\sigma_{\text{los}}^2(R) = \frac{2}{I(R)} \int_R^\infty dr \left(1 - \beta \frac{R^2}{r^2}\right) \frac{\nu \sigma_r^2 r}{\sqrt{r^2 - R^2}}. \quad (7)$$

2.3. Spherically symmetric 4th-order Jeans equations

It is important to note that LOSVDs are generally non-Gaussian even in an isotropic system where the 3-dimensional velocity distributions are Gaussian everywhere (Binney & Merrifield 1998). Hence, it is insufficient to describe LOSVDs only by the velocity dispersion alone as this case means that a non-Gaussian LOSVD is forced to be fit using the closest Gaussian distribution (see Read et al. (2021) for a demonstration). One needs other quantities that describe the degree of deviation from Gaussianity. While the 3rd-order moments correspond to the asymmetric deviation (skewness), the 4th-order moments describe the symmetric deviation from Gaussian distribution. Again, assuming a constant velocity anisotropy, the equation can be written as

$$\frac{d}{dr} \nu \overline{v_r^4} + \frac{2\beta}{r} \nu \overline{v_r^4} + 3\nu \sigma_r^2 \frac{d\Phi}{dr} = 0, \quad (8)$$

whose solution may be expressed as

$$\overline{v_r^4}(r) = \frac{3}{r^{2\beta} \nu(r)} \int_r^\infty dr' r'^{2\beta} \nu(r') \sigma_r^2(r') \frac{d\Phi}{dr'}. \quad (9)$$

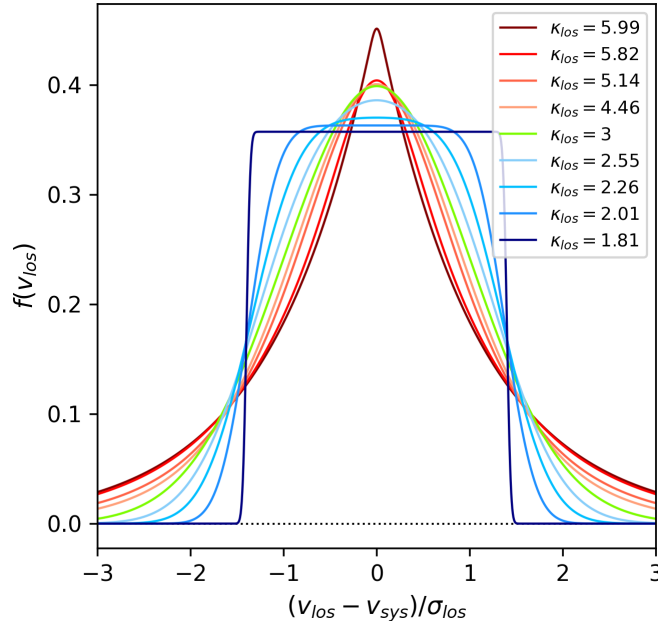


Figure 1: The changing shape of LOSVDs for different choices of κ_{los} .

The projected 4th-order moments take the form

$$\overline{v_{\text{los}}^4}(R) = \frac{2}{I(R)} \int_R^\infty dr \left[1 - 2\beta \frac{R^2}{r^2} + \frac{1}{2}\beta(1+\beta) \frac{R^4}{r^4} \right] \frac{\nu \overline{v_r^4} r}{\sqrt{r^2 - R^2}}. \quad (10)$$

It is convenient to express the 4th-order moments in the form of the line-of-sight kurtosis

$$\kappa_{\text{los}}(R) = \frac{\overline{v_{\text{los}}^4}(R)}{\sigma_{\text{los}}^4(R)}, \quad (11)$$

(Merrifield & Kent 1990; Lokas 2002) whose values are $\kappa_{\text{los}} = 3$ for a Gaussian distribution, $\kappa_{\text{los}} < 3$ for a more thin-tailed and flat-topped distribution, and $\kappa_{\text{los}} > 3$ for a spikier and more heavy-tailed distribution (see Figure 1).

In the unbinned 2nd-order only Jeans modeling, one usually links the theoretical l.o.s. velocity dispersion σ_{los} to the LOSVD by assuming that its distribution is Gaussian. Together with the velocity error measurement Δv_{los} , which has a Gaussian distribution as well, these two quantities characterize the LOSVD for each member star at position R . However, taking into account the 4th-order moments, we need to provide more freedom to the distribution function to change its shape. For this purpose, we adopt two kernels (uniform kernel and Laplacian kernel, see Appendix for details) explained in Sanders & Evans (2020) to link the theoretical l.o.s. velocity dispersion and kurtosis to the LOSVD. Figure 1 shows how the value of kurtosis changes the shape of a distribution in this model. Another notable advantage of adopting these kernels is that the velocity error measurements for each star can be convolved into the distribution. Therefore, stars with precise measurements do not lose their strong signature of kinematical information because of averaging the error or their l.o.s. velocity is unnecessary.

2.4. Fitting Procedure

In order to understand to what extent this model can recover the free parameters, we explore their most likely value by estimating the probability of each observed star via the calculated LOSVD, which is characterized by theoretical l.o.s. velocity dispersion and kurtosis. This work avoids a binned analysis because the results suffer from a strong dependency on the choice of binning and, hence, are prone to bias. The binned analysis is also avoided because extracting the observed κ_{los} by binning the sample can introduce a potentially large error of $\gtrsim 20\%$ unless each bin contains $\gtrsim 150$ stars (Merrifield & Kent 1990).

We assume that there is no net streaming motion, therefore the LOSVD is symmetrically centered at the systemic velocity of the stellar system v_{sys} . For N total number of sample stars in a stellar system, $v_{\text{los},i} \pm \delta_i$ denoting the

observed l.o.s. velocity and its uncertainty for the i -th star, the likelihood function is given by

$$L = \prod_{i=1}^N \frac{1}{(\delta_i^2 + \sigma_{\text{los},i}^2)^{1/2}} f_s(w_i), \quad (12)$$

where

$$w_i^2 = \frac{(v_{\text{los},i} - v_{\text{sys}})^2}{\delta_i^2 + \sigma_{\text{los},i}^2}, \quad (13)$$

and the choice of $f_s(w)$ is determined by the value of κ_{los} . We use the Laplacian kernel if $\kappa_{\text{los}} > 3$, the uniform kernel if $\kappa_{\text{los}} < 3$, and Gaussian kernel if $\kappa_{\text{los}} = 3$. These choices of kernel allow the shape of LOSVDs to be flexible, covering more thin-tailed to heavy-tailed distributions than a Gaussian, with the limitation being the pure uniform ($\kappa_{\text{los}} = 1.8$) and pure Laplacian ($\kappa_{\text{los}} = 6.0$) distribution at each extreme case. The theoretical velocity dispersion for the i -th star $\sigma_{\text{los},i}$ is calculated through Equation 7 at the position R_i . A flat or log-flat prior is applied to marginalize the free parameters in these given ranges:

1. $-1.0 \leq -\log_{10}(1 - \beta) \leq 1.0$,
2. $2.0 \leq \alpha \leq 10.0$,
3. $0 \leq \beta_{\text{trans}} \leq 3.0$,
4. $-2.0 \leq \gamma \leq 2.0$,
5. $-5.0 \leq \log_{10}(\rho_0) \leq 2.0$, and
6. $-2.0 \leq \log_{10}(b) \leq 2.0$.

Even though it is unphysical to have a system with $\gamma < 0$, which means a 'hole' in the center, we do not adopt a more restrictive prior range on γ that excludes the negative region. The detail concerning this selection is explained in Section 4.2.

Finally, we apply the Markov Chain Monte Carlo in the frame of the Metropolis-Hastings algorithm (Metropolis et al. 1953; Hastings 1970) to obtain the posterior distribution of the free parameters. To minimize the effects of initial conditions, we perform a burn-in process on the obtained samples.

2.5. Mock data

To test our constructed dynamical modeling, we generate mock data samples using STARSAMPLER¹ (Liu 2019). For a dark matter potential, we set two different density profiles: one is an NFW profile $(\alpha, \beta_{\text{trans}}, \gamma) = (3, 1, 1)$, and another is a cored NFW profile $(\alpha, \beta_{\text{trans}}, \gamma) = (3, 1, 0)$. The central density ρ_0 is adopted as $0.064 \times 10^9 [M_{\odot} \text{pc}^{-3}]$ for each case of DM potential.

For a light profile, we can model the stellar density profile as a Hernquist/Zhao profile (Equation 1). In this paper, we generate mock stars following a Plummer profile in a specific case of the Hernquist/Zhao profile. To this end, we set the parameters as $(\alpha_*, \beta_{\text{trans},*}, \gamma_*) = (5, 2, 0)$, where $\alpha_*, \beta_{\text{trans},*}, \gamma_*$ are the outer slope, transition sharpness, and inner slope of stellar density profile, respectively. Since the stars are embedded centrally in their respective DM halos, the parameter $b = a_{\text{dm}}/a_*$ is adopted as 10. The details of the mock data are summarized in Table 1.

Figure 2 shows the intrinsic l.o.s. velocity dispersion (left panel) and kurtosis (right panel) profile of the mock data set we generate. Turquoise lines denote the profiles for the cuspy Mock Galaxy 01, while gold lines denote the cored Mock Galaxy 02. Note from the point of view of the global stellar l.o.s. velocity dispersion,

$$\sigma_{\text{los,global}} = \sqrt{\sum_{i=1}^N \frac{(v_{\text{los},i} - v_{\text{sys}})^2}{N - 1}}, \quad (14)$$

where N is the number of sample stars. Mock Galaxy 01 global l.o.s. velocity dispersion of $\sigma_{\text{los,global}} = 8.6 \text{ km s}^{-1}$ lies in the range that is similar to the "classical" MW dSphs, e.g., Draco ($\sigma_{\text{los,global}} = 9.0_{-0.3}^{+0.3} \text{ km s}^{-1}$), Fornax

¹ <https://github.com/maoshenl/StarSampler>

Table 1: Input parameters of the mock data

Parameter	Input value in Mock Galaxy 01	Input value in Mock Galaxy 02
β	0.0	0.0
α	3.0	3.0
β_{trans}	1.0	1.0
γ	1.0	0.0
$\rho_0/[M_\odot/\text{pc}^3]$	0.064×10^9	0.064×10^9
b	10	10

($\sigma_{\text{los,global}} = 11.4_{-0.4}^{+0.4}$ km s⁻¹), Sextans ($\sigma_{\text{los,global}} = 8.4_{-0.4}^{+0.4}$ km s⁻¹), Ursa Minor ($\sigma_{\text{los,global}} = 8.0_{-0.3}^{+0.3}$ km s⁻¹). Mock Galaxy 02 with $\sigma_{\text{los,global}} = 3.3$ km s⁻¹, on the other hand, resembles the less massive category of an ultra-faint dwarf galaxy, e.g., BootesI ($\sigma_{\text{los,global}} = 2.4_{-0.5}^{+0.9}$ km s⁻¹), Coma Berenices ($\sigma_{\text{los,global}} = 4.6_{-0.8}^{+0.8}$ km s⁻¹), CraterII ($\sigma_{\text{los,global}} = 2.7_{-0.3}^{+0.3}$ km s⁻¹), SegueI ($\sigma_{\text{los,global}} = 3.7_{-1.1}^{+1.4}$ km s⁻¹) (Battaglia et al. 2022). Because of its divergent density profile in the center, $\sigma_{\text{los}}(R)$ of Mock Galaxy 01 experiences a deflection increase at some point toward the center. This is not observed in the cored Mock Galaxy 02 due to its constant and fairly lower density toward the center.

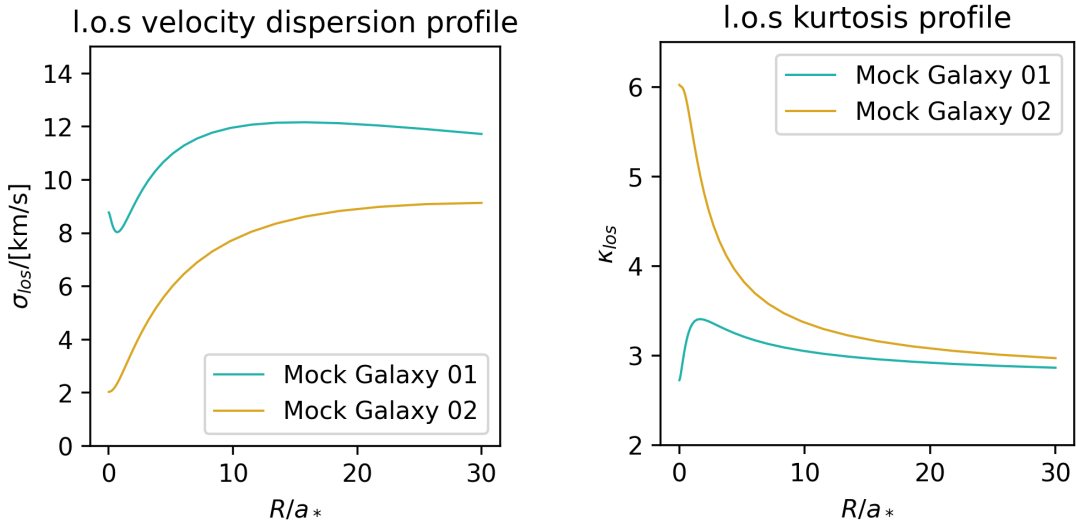


Figure 2: The left panel shows the intrinsic l.o.s. velocity dispersion as a function of the projected radius. The right panel shows the intrinsic l.o.s. kurtosis as a function of the projected radius. Each turquoise (gold) line represents the profiles of Mock Galaxy 01 (02).

The difference of γ between two mock galaxies gives the difference in the l.o.s. kurtosis profile. Despite the outer regions being relatively similar due to identical α , the inner regions exhibit a continuous divergence in $\kappa_{\text{los}}(R)$ towards the center. While $\kappa_{\text{los}}(R)$ for Mock Galaxy 01 merely departs from Gaussianity $\kappa_{\text{los}} = 3$ throughout its extent, $\kappa_{\text{los}}(R)$ for Mock Galaxy 02 significantly departs from Gaussianity toward the center, reaching $\kappa_{\text{los}} \approx 6$ in the centermost part. The large κ_{los} indicates strong tails in high v_{los} regimes and a spiky peak around $v_{\text{los}} = v_{\text{sys}}$ of the LOSVD.

3. RESULTS

In this section, we discuss results from the MCMC fitting performed using the mock data. We investigate the effects of varying the number of sample stars, velocity error measurements, and the sample star's limitation of spatial distribution. We focus on the recovery of the inner slope density and velocity anisotropy and the situation of degeneracy between them. However, the posterior distribution for all free parameters is also provided in the Appendix.

3.1. General comparison between 2nd-order only and 2nd & 4th-order fitting

Figure 3 shows the comparison of fitting based on only 2nd-order moments (the left panel) to fitting using both 2nd-order & 4th-order moments (the right panel) using 500 sample stars of Mock Galaxy 01 with velocity error $\Delta v_{\text{los}} = 2 \text{ km s}^{-1}$, resembling the typical currently available observational data set for the Milky Way’s dwarf spheroidal galaxies (Mateo et al. 2008; Walker et al. 2009a,b, 2015; Fabrizio et al. 2016; Spencer et al. 2017, 2018). The true values are $\gamma = 1.0$ and $\beta = 0.0$, marked by the red solid lines. The vertical dashed lines indicate the medians and 1σ uncertainties. In 2-dimensional posterior distributions, contour lines show 1σ and 2σ uncertainties.

While both fittings fail to assert significant constraints on γ , β is recovered within a 1σ uncertainty, with a robust exclusion of extreme tangentially and radially biased regimes. Assisted by the β -sensitive κ_{los} information, the range of error of β is reduced by about 1.5 – 2 factors after 4th-order moments are taken into account. Despite the inability to rule out the cored profile and unphysically negative γ , there is a shift toward the true value for the median value of γ . Additionally, the inclusion of 4th-order moments results in a reduction of the $\gamma - \beta$ degeneracy, as indicated by the reduction of diagonally elongated features in the 2-dimensional posterior distribution.

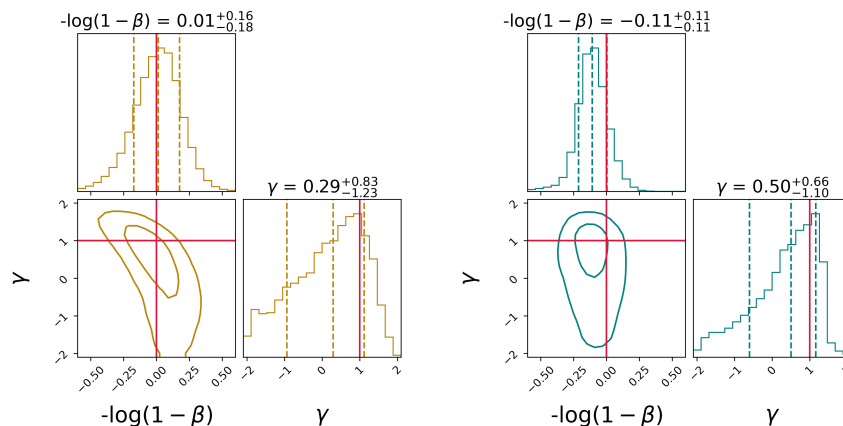


Figure 3: Posterior distributions for β and γ obtained from fitting of Mock Galaxy 01 sample stars. The left panel is 2nd-order only fitting, while the right panel is 2nd and 4th-order fitting. For both, we use 500 sample stars with 2 km s^{-1} velocity error measurement. Red solid lines indicate the true value for each parameter, and three vertical dashed lines mark the median and 1σ uncertainties. The contour lines in 2-dimensional distribution mark 1σ and 2σ uncertainties.

3.2. Effects of varying the number of samples stars

The impact of varying the number of sample stars is shown in Figure 4. We perform fittings by randomly selecting 500 stars (the left panels) and 5,000 stars (the right panels) from Mock Galaxy 01 (the upper row) and assigning $\Delta v_{\text{los}} = 2 \text{ km s}^{-1}$. Figure 4 reveals that changing the number of sample stars mainly affects the tightness of uncertainty of the free parameters’ posterior distribution. This feature is more pronounced in β where its uncertainty is shown to be reduced by a factor of ~ 3 . Notably, a similar trend of a substantial reduction in β uncertainty is observed when we fit 500 and 5,000 sample stars from Mock Galaxy 02 (the lower row), also with $\Delta v_{\text{los}} = 2.0 \text{ km s}^{-1}$. However, the lower row of Figure 4 shows a strong systematic bias for both β and γ . The inferred β is biased toward the more tangential regime, and γ is biased toward a cuspier profile than the input value. Increasing the sample size to $N = 5,000$ stars is helpless because it only reduces the random error while maintaining very similar median values, indicating that the systematic bias remains unimproved. These results suggest that it is not the number of sample stars holding the most control over this systematic bias. We explain the reason behind this bias in the next section.

3.3. Effects of varying the l.o.s. velocity measurement error

Figure 5 shows the marginalization of free parameters with different Δv_{los} for Mock Galaxy 02. In the left panel, we assign $\Delta v_{\text{los}} = 2.0 \text{ km s}^{-1}$ while in the right panel $\Delta v_{\text{los}} = 0.01 \text{ km s}^{-1}$. It is, of course, practically unachievable by the current instruments to have $\Delta v_{\text{los}} = 0.01 \text{ km s}^{-1}$. This tiny velocity error is selected in order to eliminate most of its effects to understand the model’s behavior related to velocity errors. Figure 6 is the same as Figure 5 but for Mock Galaxy 01.

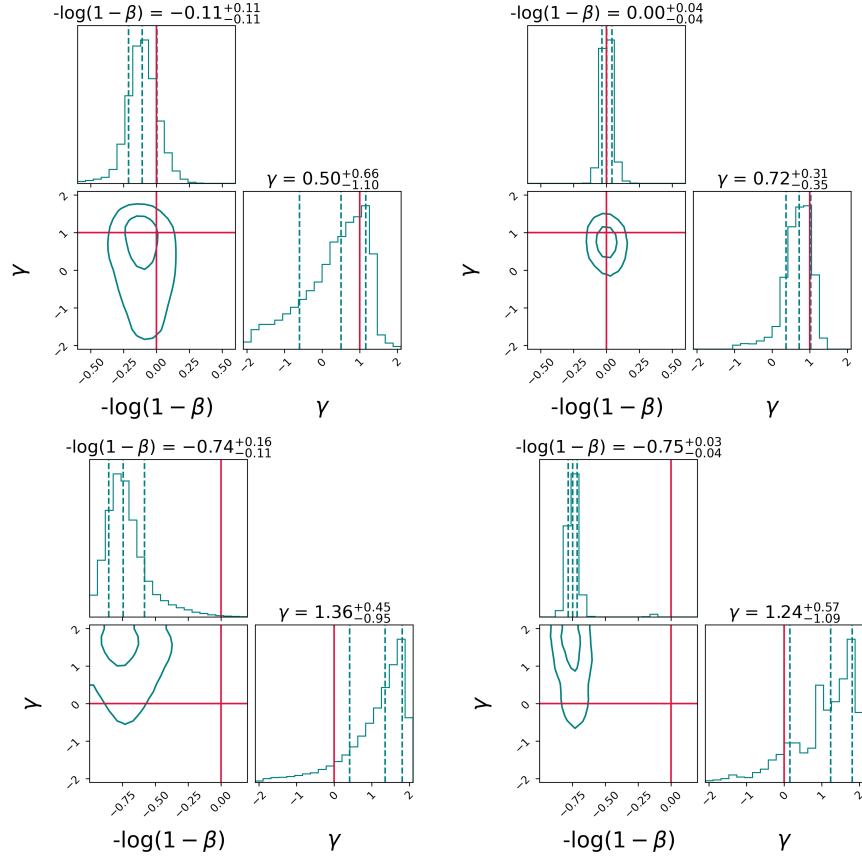


Figure 4: The same as Figure 3 but in the left panels we use 500 sample stars, while in the right panels we use 5,000 sample stars. The upper (lower) row shows the results for Mock Galaxy 01 (02). All panels are obtained from fitting using the 2nd & 4th-order moments.

We find a severe systematic bias for β and γ in the case of Mock Galaxy 02 with $\Delta v_{\text{los}} = 2.0 \text{ km s}^{-1}$ (the left panel of Figure 5). The systematic bias does not occur, however, when we push the velocity error to 0.01 km s^{-1} (the right panel of Figure 5). This velocity error-driven bias indicates the strong dependency of the 4th-order moments on the velocity distribution wings that have a small number of stars and, hence, are more severely affected by the velocity error. The departure from Gaussianity of the LOSVD, the feature that is tracked in 4th-order moments fitting, is smeared out by the velocity error that has a Gaussian distribution.

Interestingly, the dramatic change of systematic bias does not occur in Mock Galaxy 01 fitting. Figure 6 shows that varying Δv_{los} from 2.0 km s^{-1} to 0.01 km s^{-1} does not provide a considerably better result. These results from Mock Galaxy 01 and Mock Galaxy 02 fitting suggest that it is not the absolute value of Δv_{los} that matters, but the ratio of $\sigma_{\text{los,global}}/\Delta v_{\text{los}}$ instead. As long as $\sigma_{\text{los,global}} \approx \Delta v_{\text{los}}$, like the case of Mock Galaxy 02 fitting with $\Delta v_{\text{los}} = 2 \text{ km s}^{-1}$, the result will most likely be biased. However, after the ratio reaches $\sigma_{\text{los,global}}/\Delta v_{\text{los}} \approx 4$ (like the case of Mock Galaxy 01 fitting), not only the systematic bias due to the velocity error is not observed anymore, but also there is no significant improvement if we push the ratio to be larger.

To have a further test regarding this characteristic and check if the velocity error-driven bias can be addressed by increasing the number of stars, we perform a similar fitting on Mock Galaxy 01 and randomly select $N = 10^4$ stars. We assign $\sigma_{\text{los,global}}/\Delta v_{\text{los}} = 1.7$, which is very similar to the case of Mock Galaxy 02 fitting with $\Delta v_{\text{los}} = 2 \text{ km s}^{-1}$. We find that a very similar bias, where the inferred β is far more tangential and γ is cuspier than the true value, is observed. We conclude that this velocity error-driven bias cannot be reduced by increasing the sample size. Fortunately, among all the fitting, β is consistently recovered as long as $\sigma_{\text{los,global}}/\Delta v_{\text{los}} \gtrsim 4$ even though the number of sample stars is only 500 and γ is inconclusive.

3.4. Effects of varying the R_{max} of stars

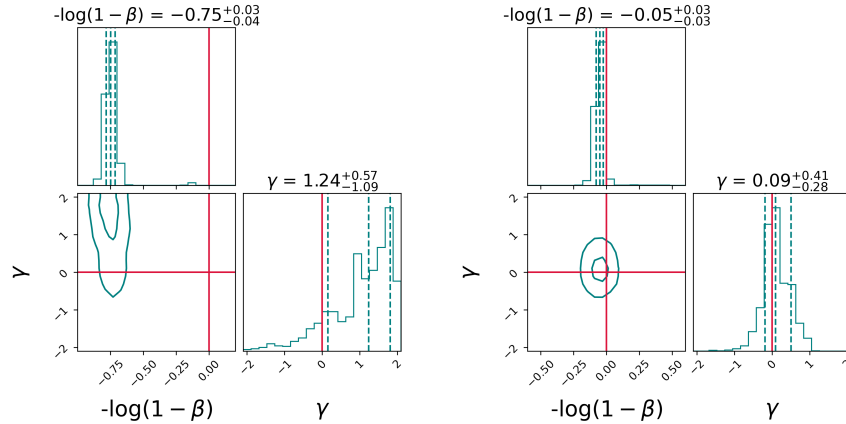


Figure 5: Posterior distributions of β and γ obtained from Mock Galaxy 02 fitting. In the left panel we assign $\Delta v_{\text{los}} = 2.0$ km s $^{-1}$, while for the right panel $\Delta v_{\text{los}} = 0.01$ km s $^{-1}$. Red solid lines indicate the input values and three vertical dashed lines mark the median and 1σ uncertainties.

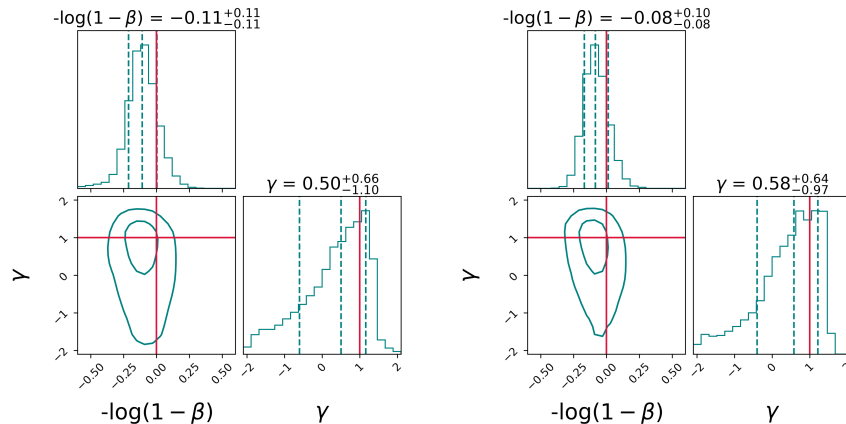


Figure 6: The same as Figure 5 but for Mock Galaxy 01.

We investigate the role of stars' spatial distribution by conducting some fittings using different values for the furthest member star available R_{max} , while fixing the Plummer scale-length a_* as well as the dark matter scale-length a_{dm} , with $b = a_{\text{dm}}/a_* = 10$. We set four different hard cuts $R_{\text{max}} = [\text{no limit}, a_{\text{dm}}, 0.5a_{\text{dm}}, 0.1a_{\text{dm}}]$ and randomly select 5,000 member stars from Mock Galaxy 02 for each R_{max} . In order not to mix with the effect from the velocity error, we fix $\Delta v_{\text{los}} = 0.01$ km s $^{-1}$.

Results of the fitting are shown in Figure 7 where it is $R_{\text{max}} = \text{no limit}$, $R_{\text{max}} = a_{\text{dm}}$, $R_{\text{max}} = 0.5a_{\text{dm}}$, and $R_{\text{max}} = 0.1a_{\text{dm}}$, respectively from left to right. Figure 7 illustrates that stars in the inner region play a dominant role in constraining γ , as evidenced by the nearly indistinguishable results among the first three leftmost panels. Moreover, the median values of γ for limited R_{max} show slightly improved performance compared to the case with no limit on R_{max} . This slight improvement is likely due to the higher number of stars in the inner part of the galaxy probing γ , a behavior that is also observed in [Chang & Necib \(2021\)](#). Only when $R_{\text{max}} = 0.1a_{\text{dm}} = a_*$ the posterior of γ shows some noticeable difference with a larger offset of the median value from the true value and a larger random error compared to the other three cases. This indicates that even though stars in the inner part of the galaxy play the main role in estimating γ , an extensive sample of at least up to $\sim 0.5a_{\text{dm}}$ is still necessary. However, a_{dm} is not observable, and we rely only on a_* to evaluate the extent of a sample set. Because of its dissipation nature, baryonic matter tends to be more centrally concentrated than dark matter ([White & Rees 1978](#); [Efstathiou & Silk 1983](#)). It is thus important to assemble sample stars beyond $R = a_*$ to place useful limits on γ

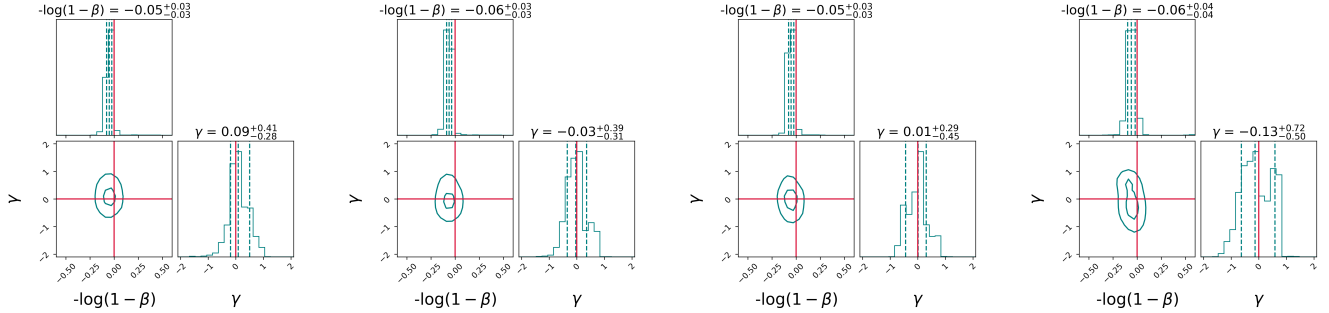


Figure 7: Posterior distributions of β and γ for Mock Galaxy 02. $R_{\max} = \text{no limit}$, $R_{\max} = a_{\text{dm}}$, $R_{\max} = 0.5a_{\text{dm}}$, and $R_{\max} = 0.1a_{\text{dm}}$, respectively from left to right. Three dashed vertical lines mark the median and 1σ uncertainties. Red solid lines are the input values of the mock data.

Figure 7 also shows that the estimation of β is consistent across all scenarios. There is no noticeable effect from changing R_{\max} nor the decreasing quality on the recovery of γ when $R_{\max} = 0.1a_{\text{dm}}$. This β and γ independency confirm the reduced degeneracy between the two parameters and different reliance on the observational properties after 4th-order moments are incorporated.

4. DISCUSSION

4.1. Dependency on the prior range

Jeans modeling has a limitation in that the solutions it provides are not guaranteed to be physically plausible. However, the prior range of γ has to be carefully selected to ensure that the results do not carry any effect from the choice. Therefore, while negative γ is physically unlikely, it is incautious if some range in $\gamma < 0$ is not included in the prior because it might suffer from the border effect. An unduly restrictive prior does not give enough solution space around $\gamma = 0$ and will force the walkers to explore $\gamma > 0$. The cored profile is thus systematically disfavoured.

We also examine if this issue has any effects when the input density profile is a cuspy halo. The result is shown in Figure 8 where we fit 5,000 randomly selected stars from Mock Galaxy 01 with two different ranges of prior on γ , i.e., a broad range $-2.0 \leq \gamma \leq 2.0$, and a narrower range of $0 \leq \gamma \leq 2.0$ that exclude the unphysical region. The shift of γ 's posterior shown in Figure 8 suggests that the issue also affects the distribution even for a cuspy true density profile. For a cuspy profile, this should not occur if the model, with the provided data, can completely exclude $\gamma < 0$. To avoid this prior-caused bias on γ , we decide to apply the broad range of prior for γ , $-2.0 \leq \gamma \leq 2.0$, for all the fittings. Prior dependency in the estimation on γ is also observed in Read et al. (2018), Genina et al. (2020), Chang & Necib (2021), and Hayashi et al. (2023b), especially for a smaller sample size.

4.2. The recovery of γ

As one of the central focuses of this work, in this subsection we discuss the recovery of γ . It is interesting to note that the case for a cored halo density profile can be recovered with a robust exclusion of the cuspy one. However, it does not occur in the cuspy case where the posterior distribution of γ does not peak at $\gamma \approx 1$ as well as there is considerable probability in the cored region. This difference can be explained by the fact that $\kappa_{\text{los}}(R)$ deviates from Gaussianity more strongly, especially in the inner part. This strong deviation gives more signatures for the 4th-order moments to exclude the incorrect regions.

Figure 9 shows the change of $\kappa_{\text{los}}(R)$ for different values of $b \equiv a_{\text{dm}}/a_*$, i.e., the ratio between the scale lengths of dark and luminous matter, in a specific γ . From left to right, the values of γ are $[0.0, 1.0, 1.5, 2.0]$, respectively. In each panel, each line denotes $b = [1, 5, 10]$, respectively, from the lightest to the darkest, while the other parameters are fixed. It is shown that in the case of the cuspy density profile, the range of $\kappa_{\text{los}}(R)$ is narrower, being more concentrated around $\kappa_{\text{los}} \approx 3$. On the other hand, the range of $\kappa_{\text{los}}(R)$ for a cored density profile is broader, reaching regions that are unlikely to be reached by a cuspy profile. Therefore, a cored halo has more opportunities to be identified more robustly than a cuspy one. The narrow range of $\kappa_{\text{los}}(R)$ in a cuspy halo also explains the more rapid decrease in all the posterior of γ for region $\gamma > 1$ compared to $\gamma < 0$. The crowded region around $\kappa_{\text{los}} \approx 3$ explains the reason for the difficulty in Mock Galaxy 01 fitting to rule out $\gamma \approx 0$. Another feature to note in Figure 9 is the

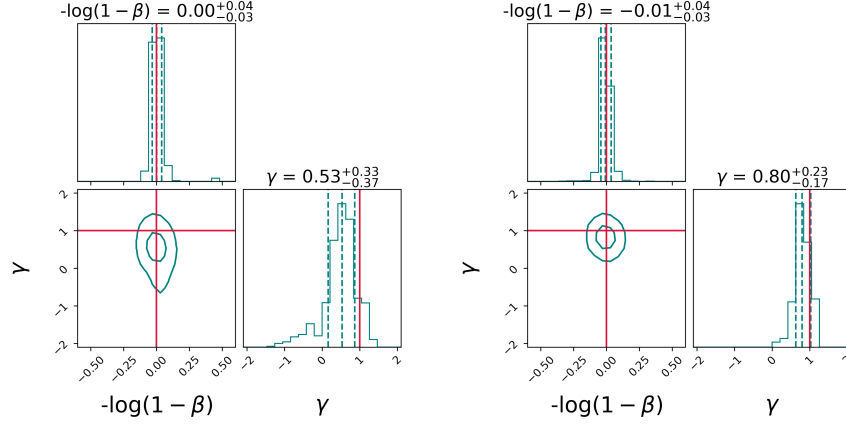


Figure 8: The same as Figure 4 but the left panel is fitting using $-2.0 \leq \gamma \leq 2.0$ and the right panel is fitting using $0 \leq \gamma \leq 2.0$ for Mock Galaxy 01. Both panels are obtained from fitting using 2nd & 4th-order moments.

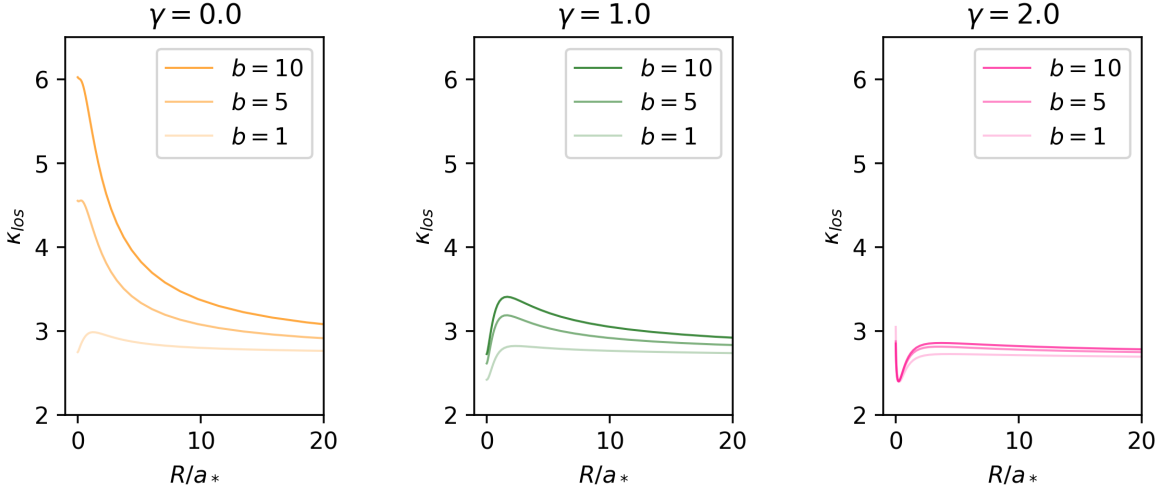


Figure 9: Different ranges of the l.o.s. kurtosis profile between DM halo with different value of b (same γ in one panel). The values are $\gamma = [0.0, 1.0, 2.0]$, respectively, from left to right. Meanwhile, the different line solidness in each panel denotes the change in b . The values are $b = [10, 5, 1]$, respectively, from the most solid line.

difference of $\kappa_{\text{los}}(R)$ between a core and a cusp with different values of b . The gap in $\kappa_{\text{los}}(R)$ between the cored and cuspy profile is more pronounced for a larger b , allowing a halo with a large b to be distinguished more easily.

Why does a cored profile obtain a more significant $\kappa_{\text{los}}(R)$ boost when b increases, compared to a cuspy profile? This can be explained by, firstly, understanding that the non-Gaussian LOSVD in a system with $\beta = 0$ is a consequence of projection, i.e., integrating velocity distribution with different values of dispersion and star count. The smallest galactocentric distance along a certain R , hence $r_{\text{min}} = R$, has the most star count in that line-of-sight. Therefore, the projected velocity dispersion at that point $\sigma_{\parallel}(r_{\text{min}})$ has the most influence in determining $\sigma_{\text{los}}(R)$. Summing up velocity distributions along the l.o.s. with a lower star count but a larger dispersion to $\sigma_{\parallel}(r_{\text{min}})$ will populate the velocity tails, resulting in a more heavy-tailed distribution than a Gaussian. The larger the ratio of $\sigma_{\parallel}(r_{\text{outer}})/\sigma_{\parallel}(r_{\text{min}})$, where $\sigma_{\parallel}(r_{\text{outer}})$ is the outermost point a member star is bound to the galaxy, the heavier the velocity tails are and hence the larger κ_{los} at that line-of-sight. This means that if $\sigma_{\parallel}(r_{\text{outer}}) < \sigma_{\parallel}(r_{\text{min}})$, then there is no region in that line-of-sight to populate the tails. Moreover, the addition of stars from $r > r_{\text{min}}$ makes the tails less significant compared to the 'central' part of the integrated velocity distribution. In this case, the resulting LOSVD has fewer outliers than a Gaussian.

Using $\sigma_{\parallel}(r_{\text{outer}})/\sigma_{\parallel}(r_{\text{min}})$ to evaluate if the resulting LOSVD has fewer or more outliers than Gaussian is, of course, a simplification and aims only to provide a general sense because $\sigma_{\parallel}(r)$ along the line-of-sight might wind up and down. The LOSVD is the net product of all contributions from each $r \geq r_{\text{min}}$. To provide more illustration, let us consider galaxies having isotropic velocity anisotropy with, again, various γ and b . Because of its isotropy, $\sigma_r(r)$ can represent any $\sigma_{\parallel}(r)$. Figure 10 shows normalized σ_r as a function of galactocentric distance scaled to a_* . The values of γ are $\gamma = [0.0, 1.0, 2.0]$, respectively, from left to right and $b = [10, 5, 1]$, respectively, from the most solid one in each panel.

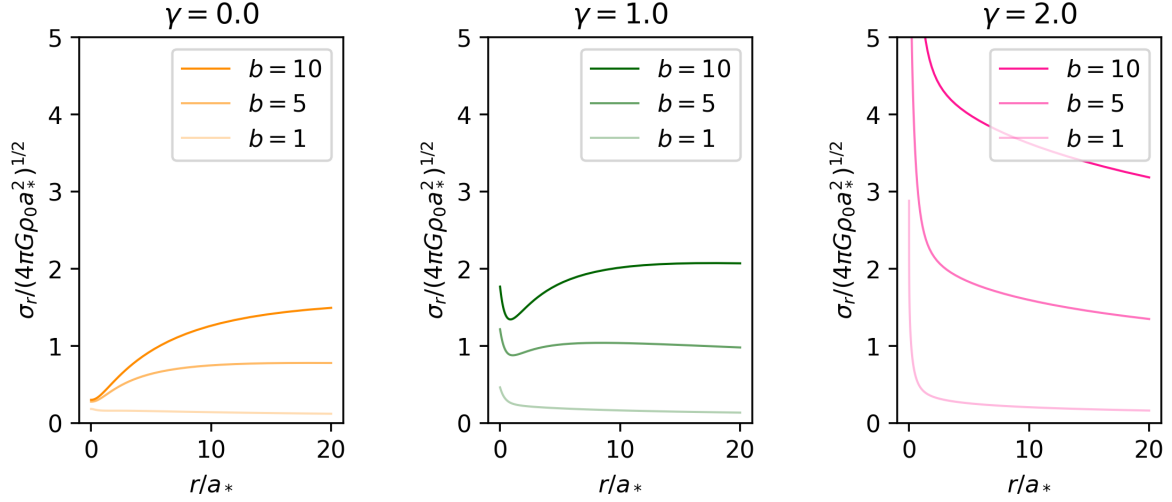


Figure 10: Normalized velocity dispersion profile in r direction for dark halo with various γ and b . The values are $\gamma = [0.0, 1.0, 2.0]$, respectively, from left to right. Different shades of line solidness in each panel denote the difference in b where $b = [10, 5, 1]$, respectively, from the most solid line.

The leftmost panel of Figure 10 shows that because of its relatively low central density, a cored profile always has a low velocity dispersion in the central part and generally increases with r , except when $b \lesssim 1$. This characteristic, on the other hand, does not exist in a cuspy profile where the velocity dispersion in the central part is relatively larger than a core and generally decreases with r . The low central velocity dispersion with a large number of stars in a core halo provides a window for stars in the outer region with higher velocity dispersion to be outliers when they are integrated along the line-of-sight to obtain the LOSVD. Furthermore, because the enclosed mass at a certain r is larger in a dark halo with a larger b , the velocity dispersion also increases more rapidly. As a result, outliers are more significant in a halo with a larger b , in agreement with the simple concept of $\sigma_{\parallel}(r_{\text{outer}})/\sigma_{\parallel}(r_{\text{min}})$ ratio. This explains two characteristics; the first one is the reason for a considerable departure from $\kappa_{\text{los}}(R) \approx 3$ for a cored dark halo with $b \gtrsim 5$ (the leftmost panel of Figure 9). The second is the reason for larger $\kappa_{\text{los}}(R)$ everywhere for a cored dark halo compared to the cuspy one with the same b (all panels in Figure 9).

Given the dependency of the estimation of γ on $\kappa_{\text{los}}(R)$, it is interesting to know if we can have an alert when the estimation is not representative or might suffer from systematic bias. However, unlike the mock data case, the intrinsic $\kappa_{\text{los}}(R)$ is not accessible in the real condition. Fortunately, star distribution in dSphs and UFDs decreases rapidly beyond a_* . Hence, calculating the κ_{los} directly from the discrete kinematics data of observed stars is heavily influenced by κ_{los} in the inner region $R < a_*$. This is enough to provide a justification if the estimation of γ might or might not be representative. In our sample sets, for example, the κ_{los} are 3.10, 3.31, 7.43, and 7.02, respectively, for Mock Galaxy 01 500 stars, Mock Galaxy 01 5,000 stars, Mock Galaxy 02 500 stars, and Mock Galaxy 02 5,000 stars. Even 500 sample stars are enough to provide a hint if $\kappa_{\text{los}}(R)$ deviates considerably from Gaussianity in some of its parts.

The estimation of γ is also challenged by a remaining degeneracy between parameters of dark matter distribution, i.e., γ , b , and ρ_0 , which might be the nature of any parametric model. Figure 11 shows $\sigma_{\text{los}}(R)$ response by varying either b (the left panel), γ (the middle panel), or ρ_0 (the right panel), while fixing the other two parameters. The values for each parameter are $b = [20, 15, 10, 5]$, $\gamma = [1.5, 1.0, 0.5, 0.0]$, and $\rho_0 = [0.2, 0.1, 0.064, 0.02] \text{ M}_{\odot} \text{ pc}^{-3}$, respectively,

from the most solid line. When fixed, we select $b = 10$, $\gamma = 1.0$, and $\rho_0 = 0.064 \text{ M}_\odot \text{ pc}^{-3}$. In Figure 12, the left panel shows the effect on $\kappa_{\text{los}}(R)$ by varying $b = [10, 5, 3, 1]$, respectively, from the most solid line while holding $\gamma = 0.0$. In the right panel we change $\gamma = [0.0, 0.5, 1.0, 1.5]$, respectively, from the most solid line while holding $b = 10$. Note that $\kappa_{\text{los}}(R)$ does not depend on ρ_0 , leaving the estimation of ρ_0 completely relies on the 2nd-order moment $\sigma_{\text{los}}(R)$ fitting. The similar response of $\sigma_{\text{los}}(R)$ and $\kappa_{\text{los}}(R)$ to changes in b , γ , or ρ_0 contributes to the difficulties in ruling out the incorrect values of γ , especially in the case of $\gamma = 1.0$.

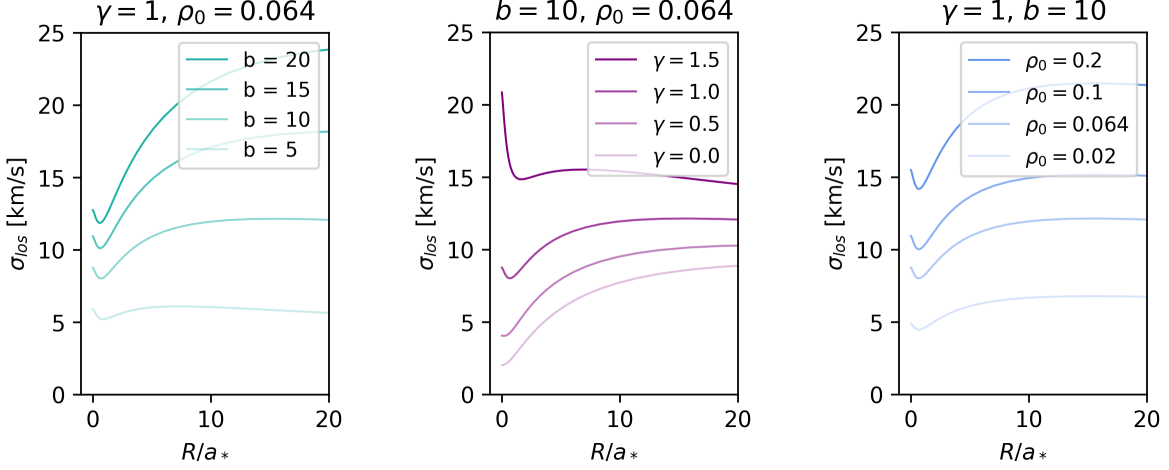


Figure 11: The line-of-sight velocity dispersion profile of dark halos with a fixed $\gamma = 0.0$ and $\rho_0 = 0.064 \text{ M}_\odot \text{ pc}^{-3}$ but varying $b = [20, 15, 10, 5]$ in the left panel, a fixed $b = 10$ and $\rho_0 = 0.064 \text{ M}_\odot \text{ pc}^{-3}$ but varying $\gamma = [1.5, 1.0, 0.5, 0.0]$ in the middle panel, and a fixed $\gamma = 1.0$ and $b = 10$ while changing $\rho_0 = [0.2, 0.1, 0.064, 0.02] \text{ M}_\odot \text{ pc}^{-3}$ in the right panel, respectively, from the most solid line.

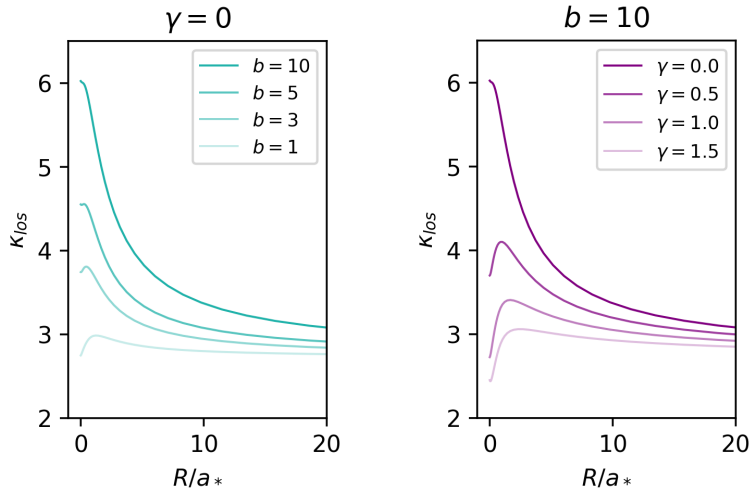


Figure 12: The line-of-sight kurtosis profile of dark halos with a fixed $\gamma = 0.0$ but varying $b = [10, 5, 3, 1]$ in the left panel, and a fixed $b = 10$ but varying $\gamma = [0.0, 0.5, 1.0, 1.5]$ in the right panel, respectively, from the most solid line.

4.3. The recovery of β

Although the situation in the recovery of γ is not simple, Figure 3 to 7 show that this model can consistently recover β within 1σ uncertainty as long as $\sigma_{\text{los,global}}/\Delta v_{\text{los}} \gtrsim 4$, without any noticeable dependency on the recovery of γ . This recovery of β is achieved even if the sample size is only as small as 500 stars and remains unaffected even when the

kinematics sample extends only in the inner region $\sim 0.1a_{\text{dm}}$. The consistent recovery of β suggests the uniqueness of β influence on $\kappa_{\text{los}}(R)$ compared to the other parameters.

Figure 13 shows the behavior of $\kappa_{\text{los}}(R)$ when β changes. From the leftmost panel, the values of β are -0.5, 0.0, and 0.5, respectively. Meanwhile, lines colored in orange, green, and pink denote different values of the dark matter inner density slope $\gamma = [0.0, 1.0, 2.0]$, respectively. We fix the ratio of dark matter scale length to light scale length as $b = 10$ in all panels.

From the previous section, we understand that increasing γ results in more flat-topped LOSVDs with fewer outliers. This happens because the larger velocity dispersion pushes stars away from $v_{\text{los}} \approx v_{\text{sys}}$ in high stellar density regions. By contrast, as illustrated in Figure 13, increasing β decreases $\kappa_{\text{los}}(R)$ in the inner region but increases it in the outer region, according to the light and mass profiles adopted in our model. This different response of $\kappa_{\text{los}}(R)$ to changes in β and γ is the main reason for the disentanglement in the estimation of the two parameters. Models relying solely on 2nd-order moments have no access to this distinction because increasing β or γ leads to an increase in $\sigma_{\text{los}}(R)$, especially in $R < a_{\text{dm}}$. Moreover, unlike a large γ that produces a narrow range of $\kappa_{\text{los}}(R)$ as shown in Figure 9, β has no regime that confines $\kappa_{\text{los}}(R)$ in a similar restriction. Even in the most subtle response of $\kappa_{\text{los}}(R)$, that occurs when $\beta = 0$, $\kappa_{\text{los}}(R)$ is allowed to lie in a relatively wide range $2 \lesssim \kappa_{\text{los}}(R) \lesssim 6$ as shown in the middle panel in Figure 13. Thus, the model finds it less challenging to rule out incorrect values of β than those of γ . Overall, $\kappa_{\text{los}}(R)$ is more sensitive to changes in β than to changes in γ , particularly in the case of large γ . This sensitivity is the main reason why applying a higher-order moment analysis is able to place tight constraints on β .

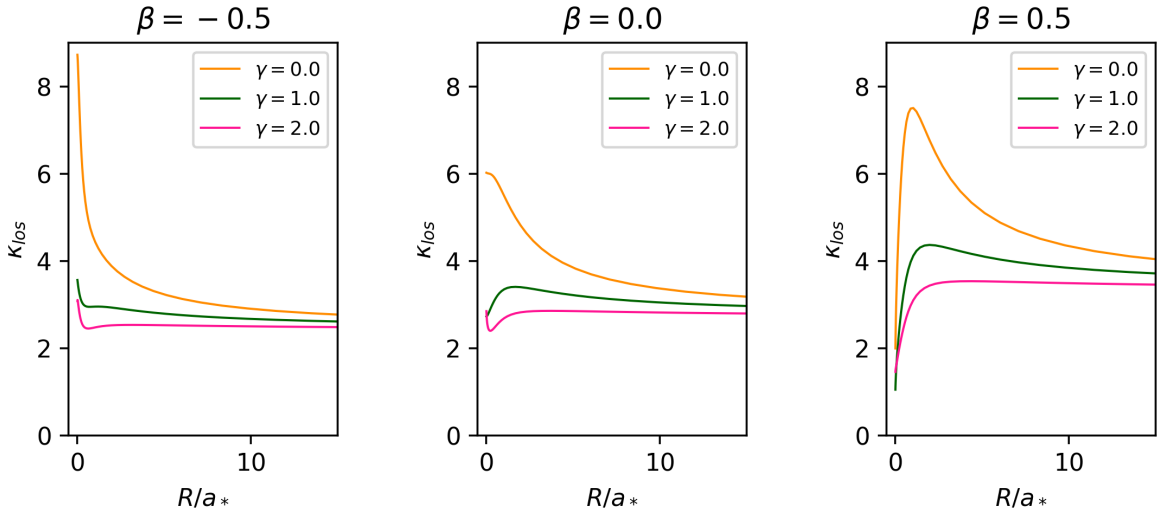


Figure 13: The line-of-sight kurtosis profile of dark halos with a fixed $b = 10$ but different values of β and γ . The values are $\beta = [-0.5, 0.0, 0.5]$, respectively, from left to right. Orange, green, and pink lines denote $\gamma = [0.0, 1.0, 2.0]$, respectively.

The common trend of increasing $\kappa_{\text{los}}(R)$ with increasing β in the outer region $R \gtrsim a_{\text{dm}} \approx 10a_*$ can be explained by considering a line-of-sight in that region. The stellar density in this region drops rapidly as $\nu(r) \propto r^{-5}$. Therefore, any l.o.s. will be highly dominated by the stars located around the closest point of the l.o.s. to the galactic center $r_{\text{min}} = R$. In a system with $\beta > 0$, this point is filled by stars with $v_{\text{los}} \approx v_{\text{sys}}$, resulting in a strong-peaked LOSVD around $v_{\text{los}} = v_{\text{sys}}$ and, hence, a large κ_{los} . Meanwhile, for a system with $\beta < 0$, this point is filled by a diverse value of v_{\parallel} from stars with nearly circular orbits with different inclinations, resulting in a broad and flat-topped LOSVD. A similar behavior is mentioned by Binney & Tremaine (2008) for a Hernquist density model for both light and mass profiles. In addition, along any line-of-sight, the velocity ellipsoid component parallel to the line of sight, $\sigma_{\parallel}(r)$, is always more aligned to $\sigma_r(r)$ with increasing r . Because of this reason, high v_{los} stars in $r \gg r_{\text{min}}$ populate the LOSVD tails in a system with radially biased orbits. However, it does not occur in a system with tangentially biased orbits because the l.o.s. cuts stars' orbits at approximately right angles.

The behavior of $\kappa_{\text{los}}(R)$ in the inner region is more complex due to the interplay between the dark matter density profile and stellar density. Instead of being heavily dominated by stars in r_{min} , the integrated LOSVD is more

dominated by stars lying in front of or behind r_{\min} because of the shallow stellar density gradient. Because of that, contribution to v_{los} in these regions is mainly obtained from the radial component of the star’s orbital velocity. If $\beta < 0$, most of the stars in those regions have $v_{\text{los}} \approx v_{\text{sys}}$, resulting in a strong spike around $v_{\text{los}} = v_{\text{sys}}$ in the LOSVD and a large κ_{los} . If $\beta > 0$, the LOSVD is filled by stars with various v_{los} from the radial velocity of stars with different galactocentric distances. This effect produces a broad, flat-topped LOSVD and a small κ_{los} .

The more sensitive response of $\kappa_{\text{los}}(R)$ in a system with $\beta \neq 0$ suggests that the estimation of free parameters can be achieved more robustly than in $\beta = 0$ case. However, using different mass modeling methods, [Read et al. \(2021\)](#) find that it is more challenging to recover the density and velocity anisotropy in systems with $\beta > 0$ than systems with $\beta \leq 0$. [Merrifield & Kent \(1990\)](#) also suggest that the number of stars required to recover kurtosis in a heavy-tailed distribution is significantly larger than in a more thin-tailed distribution. One more thing to note is our assumption that $\beta(r) = \text{constant}$. In reality, β might change with r as suggested by various studies. For example, [Loebman et al. \(2018\)](#) simulate Milky Way-sized galaxies and observed a tendency for $\beta \sim 0$ in the innermost regions, changing to a radially biased $\beta \sim 0.7$ in the outer regions. Meanwhile, [Kowalczyk et al. \(2019\)](#) apply a spherically symmetric Schwarzschild orbit superposition method to the Fornax dSph. Using this method, which does not require any assumption on the shape of $\beta(r)$, they find $\beta \approx 0$ in the center and mildly decreases with radius. Therefore, a careful study of systems with $\beta \neq 0$ as well as non-constant β is necessary.

5. CONCLUSIONS

We construct a dynamical model for dwarf spheroidal and ultra-faint dwarf galaxies under the frame of 2nd-order and 4th-order spherical Jeans equations. Assuming that the velocity anisotropy β is constant with the galactocentric distance and negligible stellar mass compared to dark mass, the model is examined using two sets of mock galaxies, one cuspy and the other cored, to investigate its behavior and ability to break mass-anisotropy degeneracy. To show the effects of some observational limitations, we have performed fittings with different values of a number of sample stars, l.o.s. velocity error measurements, and spatial distribution of the sample. We also conduct fittings where only 2nd-order moments are taken into account.

The results of our fitting show that the incorporation of 4th-order moments disentangles β from γ . It partially reduces the degeneracy between the two parameters compared to the situation when only 2nd-order moments are taken into account. The heavy reliance of 4th-order moments on the tails of the velocity distribution, where the star count is low, makes it prone to velocity error measurements. We find that in this model, β is consistently recovered within 1σ uncertainty as long as the ratio $\sigma_{\text{los,global}}/\Delta v_{\text{los}} \gtrsim 4$ is satisfied, even when the sample size is as small as 500 stars. While the ratio $\sigma_{\text{los,global}}/\Delta v_{\text{los}}$ holds the most control on the systematic bias, the number of stars affects the most on the tightness of posterior distribution. However, even though this model succeeds in reproducing the input value of β , the condition for γ is not as simple. The successful recovery of β is mainly aided by $\kappa_{\text{los}}(R)$ ’s sensitivity to the change in β . The milder response of $\kappa_{\text{los}}(R)$ to changes in γ results in a less strict constraint on γ . We find that the incorrect value of γ can be ruled out more robustly as $\kappa_{\text{los}}(R)$ deviates more from 3. This happens because of the existence of degeneracy between $\gamma - a_{\text{dm}} - \rho_0$ and the fact that if κ_{los} is far from 3, any change of these parameters changes κ_{los} more dramatically compared to when $\kappa_{\text{los}} \approx 3$.

The challenging situation when $\kappa_{\text{los}} \approx 3$ indicates the importance of relaxing the assumption of sphericity to step forward and adopt a more realistic condition. In an axisymmetric model, for example, different l.o.s. velocity dispersion profiles are imprinted along the projected major and minor axes with also distinguishable responses between a core and a cusp ([Hayashi & Chiba 2012](#)). Although the behavior of the l.o.s. kurtosis in the axisymmetric model remains unexplored, incorporating these signatures is expected to enable more stringent estimations to uncover the actual density profile in dwarf galaxies. Moreover, the support for the non-spherical model is reinforced by both observations and simulations. It is noted that the light distribution in dSphs and UFDs is not spherically symmetry ([Muñoz et al. 2018](#); [Battaglia et al. 2022](#)). From the theoretical side, results from CDM simulations show that dark halos are generally non-spherical ([Allgood et al. 2006](#); [Orkney et al. 2023](#)).

In this work, we only consider conditions where the membership of a star can be determined perfectly. However, working with observational data has to face the challenge of contamination from foreground or unbound stars ([Battaglia et al. 2013](#)). While a detailed study of contamination effects is beyond the scope of this paper, the use of kurtosis is more prone to these contaminations compared to the model using only the 2nd-order moments, especially if those stars fall in the tails of LOSVDs ([Merrifield & Kent 1990](#)). The role of binaries also needs to be properly taken into account. Although it is suggested that the contribution of binaries in inflating the velocity dispersion profile in dSphs

is insignificant and to be carefully treated if we work with UFDs (Minor 2013; Spencer et al. 2017; Arroyo-Polonio et al. 2023; Wang et al. 2023), a quantitative approach of unresolved binaries influence on $\kappa_{\text{los}}(R)$ is to be studied in future work.

- 1 We are grateful to Laszlo Dobos, Carrie Filion, Evan Kirby, Alex Szalay, Rosie Wyse, and the Subaru/PFS GA
 2 working group for their useful discussion on the derivation and analysis of the LOSVD of dwarf satellites. This
 3 work was supported in part by the MEXT Grant-in-Aid for Scientific Research (No. JP20H01895, JP21K13909, and
 4 JP23H04009 for KH, No. JP18H05437, JP21H05448, and JP24K00669 for MC.).

APPENDIX

A. KERNELS

A.1. Uniform Kernel

To produce a distribution that is more boxy, having fewer outliers than a Gaussian distribution and a flat-topped peak, we can use the uniform kernel (Sanders & Evans 2020)

$$K_+(y) = \frac{1}{2a}, \text{ if } y < a. \quad (\text{A1})$$

The error-convolved distribution is

$$f_s(w) = \frac{b}{2a} \left[\Phi\left(\frac{bw+a}{t}\right) - \Phi\left(\frac{bw-a}{t}\right) \right], \quad (\text{A2})$$

with

$$t^2 = 1 + b^2\delta^2, \quad (\text{A3})$$

$$b^2 = 1 + \frac{a^2}{k^2}, \quad (\text{A4})$$

$$k(a) = k_0 - (k_0 - k_\infty) \tanh\left(\frac{a}{a_0}\right), \quad (\text{A5})$$

$$\kappa = -\frac{2a^4}{15} \left(1 + \frac{a^2}{3}\right)^{-2} + 3, \quad (\text{A6})$$

where δ is the velocity error measurement and $\Phi(x)$ is the cumulative distribution function for the unit Gaussian PDF

$$\Phi(x) = \frac{1}{\sqrt{2\pi}} \int_{-\infty}^x dt \exp\left(-\frac{t^2}{2}\right). \quad (\text{A7})$$

The value for some appearing constants are $a_0 = 3.3$, $k_0 = \sqrt{3}$, $k_\infty \approx 7/5$. This kernel can produce distributions with kurtosis lying in the range of $1.8 \leq \kappa < 3.0$.

A.2. Laplacian Kernel

To produce a distribution with more outliers than a Gaussian distribution, more heavy-tailed and a spikier peak, we can use the Laplacian kernel (Sanders & Evans 2020)

$$K_+(y) = \frac{1}{2a} \exp\left(-\frac{y}{a}\right). \quad (\text{A8})$$

The error-convolved distribution is

$$f_s = \frac{b}{4a} \exp\left(\frac{t^2 - 2abw}{2a^2}\right) \operatorname{erfc}\left(\frac{t^2 - abw}{\sqrt{2}ta}\right) + \frac{b}{4a} \exp\left(\frac{t^2 + 2abw}{2a^2}\right) \operatorname{erfc}\left(\frac{t^2 + abw}{\sqrt{2}ta}\right), \quad (\text{A9})$$

$$\kappa = \frac{12a^4}{(2a^2 + 1)^2} + 3, \quad (\text{A10})$$

with the same relation as Equation A3, A4, A5 for t , b , k , respectively. The value for some appearing constants are $a_0 = 2.25$, $k_0 = 1/\sqrt{2}$, $k_{\infty,0} = 1.08$. This kernel can produce distributions with kurtosis lying in the range of $3.0 < \kappa \leq 6.0$.

B. ALL FREE PARAMETERS

Figure 14 shows the posterior distribution for all six free parameters in our estimation. From left to right they are β , α , β_{trans} , γ , ρ_0 , and b . The upper panel is Mock Galaxy 01, and the lower panel is Mock Galaxy 02. Both panels are obtained using 5,000 sample stars from each mock galaxy, involving 2nd-order and 4th-order moments. Red lines indicate the mock galaxy’s input values, while three vertical dashed lines mark the median and 1σ uncertainty. Correlations between b , γ , and ρ_0 appear in the 2-dimensional distribution indicated by the diagonally elongated contours.

REFERENCES

- Allgood, B., Flores, R. A., Primack, J. R., et al. 2006, *MNRAS*, 367, 1781, doi: [10.1111/j.1365-2966.2006.10094.x](https://doi.org/10.1111/j.1365-2966.2006.10094.x)
- Amorisco, N. C., & Evans, N. W. 2012, *MNRAS*, 419, 184, doi: [10.1111/j.1365-2966.2011.19684.x](https://doi.org/10.1111/j.1365-2966.2011.19684.x)
- Arroyo-Polonio, J. M., Battaglia, G., Thomas, G. F., et al. 2023, *A&A*, 677, A95, doi: [10.1051/0004-6361/202346843](https://doi.org/10.1051/0004-6361/202346843)
- Battaglia, G., Helmi, A., & Breddels, M. 2013, *NewAR*, 57, 52, doi: [10.1016/j.newar.2013.05.003](https://doi.org/10.1016/j.newar.2013.05.003)
- Battaglia, G., & Nipoti, C. 2022, *Nature Astronomy*, 6, 659, doi: [10.1038/s41550-022-01638-7](https://doi.org/10.1038/s41550-022-01638-7)
- Battaglia, G., Taibi, S., Thomas, G. F., & Fritz, T. K. 2022, *A&A*, 657, A54, doi: [10.1051/0004-6361/202141528](https://doi.org/10.1051/0004-6361/202141528)
- Binney, J., & Merrifield, M. 1998, *Galactic Astronomy*
- Binney, J., & Tremaine, S. 2008, *Galactic Dynamics: Second Edition*
- Breddels, M. A., Helmi, A., van den Bosch, R. C. E., van de Ven, G., & Battaglia, G. 2013, *MNRAS*, 433, 3173, doi: [10.1093/mnras/stt956](https://doi.org/10.1093/mnras/stt956)
- Bullock, J. S., & Boylan-Kolchin, M. 2017, *ARA&A*, 55, 343, doi: [10.1146/annurev-astro-091916-055313](https://doi.org/10.1146/annurev-astro-091916-055313)
- Burkert, A. 1995, *ApJL*, 447, L25, doi: [10.1086/309560](https://doi.org/10.1086/309560)
- Chang, L. J., & Necib, L. 2021, *MNRAS*, 507, 4715, doi: [10.1093/mnras/stab2440](https://doi.org/10.1093/mnras/stab2440)
- de Blok, W. J. G. 2010, *Advances in Astronomy*, 2010, 789293, doi: [10.1155/2010/789293](https://doi.org/10.1155/2010/789293)
- Efstathiou, G., & Silk, J. 1983, *FCPh*, 9, 1
- Fabrizio, M., Bono, G., Nonino, M., et al. 2016, *ApJ*, 830, 126, doi: [10.3847/0004-637X/830/2/126](https://doi.org/10.3847/0004-637X/830/2/126)
- Flores, R. A., & Primack, J. R. 1994, *ApJL*, 427, L1, doi: [10.1086/187350](https://doi.org/10.1086/187350)
- Genina, A., Read, J. I., Frenk, C. S., et al. 2020, *MNRAS*, 498, 144, doi: [10.1093/mnras/staa2352](https://doi.org/10.1093/mnras/staa2352)
- Geringer-Sameth, A., Koushiappas, S. M., & Walker, M. 2015, *ApJ*, 801, 74, doi: [10.1088/0004-637X/801/2/74](https://doi.org/10.1088/0004-637X/801/2/74)
- Hagen, J. H. J., Helmi, A., & Breddels, M. A. 2019, *A&A*, 632, A99, doi: [10.1051/0004-6361/201936196](https://doi.org/10.1051/0004-6361/201936196)
- Hastings, W. K. 1970, *Biometrika*, 57, 97, doi: [10.1093/biomet/57.1.97](https://doi.org/10.1093/biomet/57.1.97)
- Hayashi, K., & Chiba, M. 2012, *ApJ*, 755, 145, doi: [10.1088/0004-637X/755/2/145](https://doi.org/10.1088/0004-637X/755/2/145)
- . 2015, *ApJ*, 810, 22, doi: [10.1088/0004-637X/810/1/22](https://doi.org/10.1088/0004-637X/810/1/22)
- Hayashi, K., Chiba, M., & Ishiyama, T. 2020, *ApJ*, 904, 45, doi: [10.3847/1538-4357/abbe0a](https://doi.org/10.3847/1538-4357/abbe0a)
- Hayashi, K., Dobos, L., Filion, C., et al. 2023a, *arXiv e-prints*, arXiv:2305.11309, doi: [10.48550/arXiv.2305.11309](https://doi.org/10.48550/arXiv.2305.11309)
- Hayashi, K., Hirai, Y., Chiba, M., & Ishiyama, T. 2023b, *ApJ*, 953, 185, doi: [10.3847/1538-4357/ace33e](https://doi.org/10.3847/1538-4357/ace33e)
- Hernquist, L. 1990, *ApJ*, 356, 359, doi: [10.1086/168845](https://doi.org/10.1086/168845)
- Jardel, J. R., & Gebhardt, K. 2012, *ApJ*, 746, 89, doi: [10.1088/0004-637X/746/1/89](https://doi.org/10.1088/0004-637X/746/1/89)
- Jardel, J. R., Gebhardt, K., Fabricius, M. H., Drory, N., & Williams, M. J. 2013, *ApJ*, 763, 91, doi: [10.1088/0004-637X/763/2/91](https://doi.org/10.1088/0004-637X/763/2/91)
- Kowalczyk, K., del Pino, A., Lokas, E. L., & Valluri, M. 2019, *MNRAS*, 482, 5241, doi: [10.1093/mnras/sty3100](https://doi.org/10.1093/mnras/sty3100)
- Kowalczyk, K., & Lokas, E. L. 2022, *A&A*, 659, A119, doi: [10.1051/0004-6361/202142212](https://doi.org/10.1051/0004-6361/202142212)
- Liu, M. S. 2019, PhD thesis, Carnegie Mellon University, Pennsylvania
- Loebman, S. R., Valluri, M., Hattori, K., et al. 2018, *ApJ*, 853, 196, doi: [10.3847/1538-4357/aaa0d6](https://doi.org/10.3847/1538-4357/aaa0d6)
- Lokas, E. L. 2002, *MNRAS*, 333, 697, doi: [10.1046/j.1365-8711.2002.05457.x](https://doi.org/10.1046/j.1365-8711.2002.05457.x)
- . 2009, *MNRAS*, 394, L102, doi: [10.1111/j.1745-3933.2009.00620.x](https://doi.org/10.1111/j.1745-3933.2009.00620.x)
- Mateo, M., Olszewski, E. W., & Walker, M. G. 2008, *ApJ*, 675, 201, doi: [10.1086/522326](https://doi.org/10.1086/522326)
- Merrifield, M. R., & Kent, S. M. 1990, in *Bulletin of the American Astronomical Society*, Vol. 22, 744
- Metropolis, N., Rosenbluth, A. W., Rosenbluth, M. N., Teller, A. H., & Teller, E. 1953, *JChPh*, 21, 1087, doi: [10.1063/1.1699114](https://doi.org/10.1063/1.1699114)
- Minor, Q. E. 2013, *ApJ*, 779, 116, doi: [10.1088/0004-637X/779/2/116](https://doi.org/10.1088/0004-637X/779/2/116)
- Moore, B. 1994, *Nature*, 370, 629, doi: [10.1038/370629a0](https://doi.org/10.1038/370629a0)
- Muñoz, R. R., Côté, P., Santana, F. A., et al. 2018, *ApJ*, 860, 66, doi: [10.3847/1538-4357/aac16b](https://doi.org/10.3847/1538-4357/aac16b)

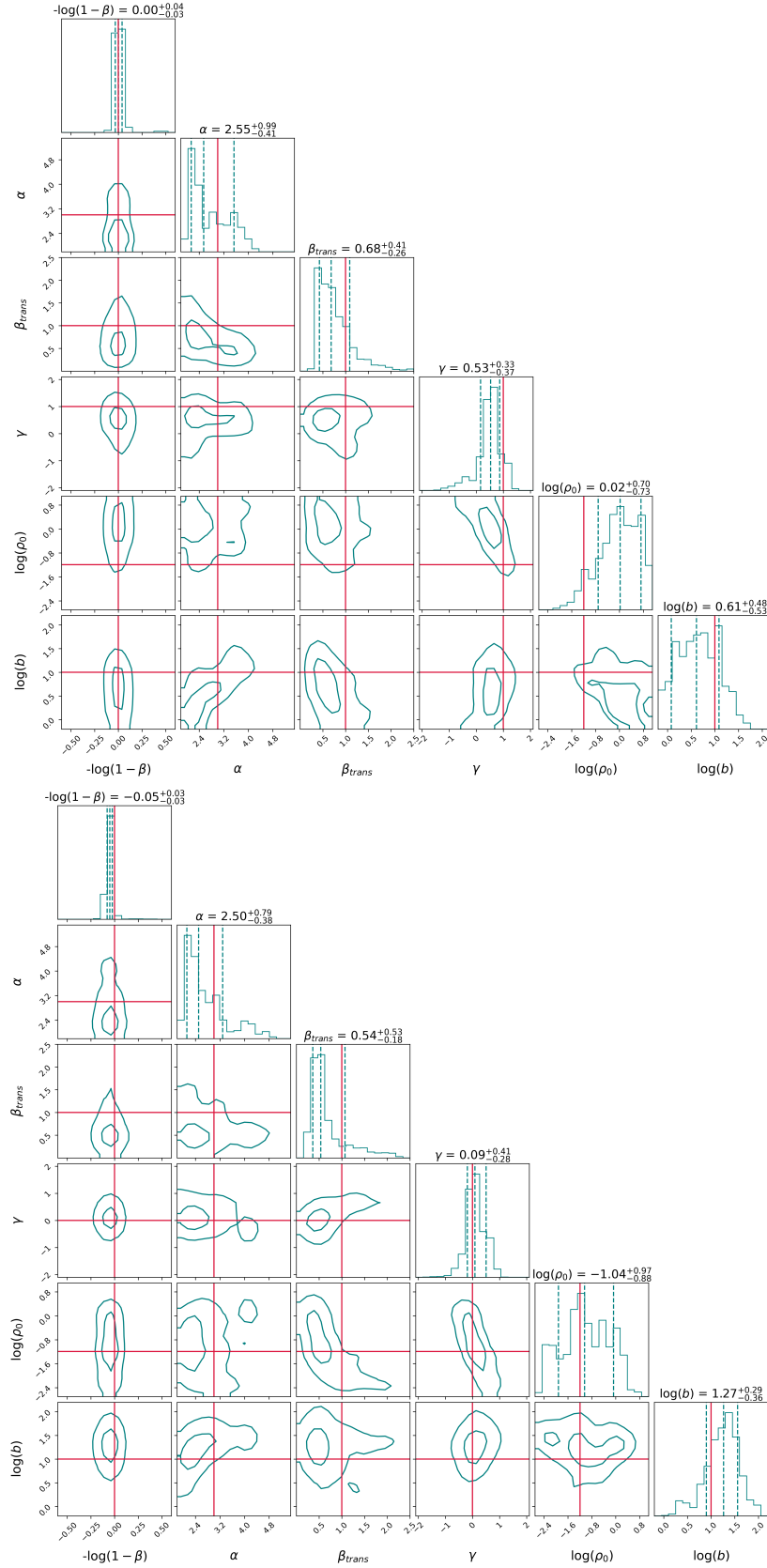


Figure 14: Posterior distributions for all six free parameters obtained using $N = 5,000$ stars with both 2nd-order and 4th-order moments. The upper panel is Mock Galaxy 01, and the lower panel is Mock Galaxy 02. Red lines indicate the input values for each parameter, while vertical dashed lines mark the median and 1σ uncertainties.

- Navarro, J. F., Eke, V. R., & Frenk, C. S. 1996, *MNRAS*, 283, L72, doi: [10.1093/mnras/283.3.L72](https://doi.org/10.1093/mnras/283.3.L72)
- Oh, S.-H., Hunter, D. A., Brinks, E., et al. 2015, *AJ*, 149, 180, doi: [10.1088/0004-6256/149/6/180](https://doi.org/10.1088/0004-6256/149/6/180)
- Orkney, M. D. A., Taylor, E., Read, J. I., et al. 2023, *MNRAS*, 525, 3516, doi: [10.1093/mnras/stad2516](https://doi.org/10.1093/mnras/stad2516)
- Plummer, H. C. 1911, *MNRAS*, 71, 460, doi: [10.1093/mnras/71.5.460](https://doi.org/10.1093/mnras/71.5.460)
- Read, J. I., Walker, M. G., & Steger, P. 2018, *MNRAS*, 481, 860, doi: [10.1093/mnras/sty2286](https://doi.org/10.1093/mnras/sty2286)
- Read, J. I., Mamon, G. A., Vasiliev, E., et al. 2021, *MNRAS*, 501, 978, doi: [10.1093/mnras/staa3663](https://doi.org/10.1093/mnras/staa3663)
- Richardson, T., & Fairbairn, M. 2013, *MNRAS*, 432, 3361, doi: [10.1093/mnras/stt686](https://doi.org/10.1093/mnras/stt686)
- . 2014, *MNRAS*, 441, 1584, doi: [10.1093/mnras/stu691](https://doi.org/10.1093/mnras/stu691)
- Sanders, J. L., & Evans, N. W. 2020, *MNRAS*, 499, 5806, doi: [10.1093/mnras/staa2860](https://doi.org/10.1093/mnras/staa2860)
- Simon, J. D. 2019, *ARA&A*, 57, 375, doi: [10.1146/annurev-astro-091918-104453](https://doi.org/10.1146/annurev-astro-091918-104453)
- Spencer, M. E., Mateo, M., Olszewski, E. W., et al. 2018, *AJ*, 156, 257, doi: [10.3847/1538-3881/aae3e4](https://doi.org/10.3847/1538-3881/aae3e4)
- Spencer, M. E., Mateo, M., Walker, M. G., & Olszewski, E. W. 2017, *ApJ*, 836, 202, doi: [10.3847/1538-4357/836/2/202](https://doi.org/10.3847/1538-4357/836/2/202)
- Takada, M., Ellis, R. S., Chiba, M., et al. 2014, *PASJ*, 66, R1, doi: [10.1093/pasj/pst019](https://doi.org/10.1093/pasj/pst019)
- Tamura, N., Takato, N., Shimono, A., et al. 2016, in *Society of Photo-Optical Instrumentation Engineers (SPIE) Conference Series*, Vol. 9908, *Ground-based and Airborne Instrumentation for Astronomy VI*, ed. C. J. Evans, L. Simard, & H. Takami, 99081M, doi: [10.1117/12.2232103](https://doi.org/10.1117/12.2232103)
- Walker, M. G., Mateo, M., & Olszewski, E. W. 2009a, *AJ*, 137, 3100, doi: [10.1088/0004-6256/137/2/3100](https://doi.org/10.1088/0004-6256/137/2/3100)
- Walker, M. G., Mateo, M., Olszewski, E. W., Sen, B., & Woodroffe, M. 2009b, *AJ*, 137, 3109, doi: [10.1088/0004-6256/137/2/3109](https://doi.org/10.1088/0004-6256/137/2/3109)
- Walker, M. G., Olszewski, E. W., & Mateo, M. 2015, *VizieR Online Data Catalog*, *J/MNRAS/448/2717*
- Walker, M. G., & Peñarrubia, J. 2011, *ApJ*, 742, 20, doi: [10.1088/0004-637X/742/1/20](https://doi.org/10.1088/0004-637X/742/1/20)
- Wang, W., Zhu, L., Jing, Y., et al. 2023, *ApJ*, 956, 91, doi: [10.3847/1538-4357/acf314](https://doi.org/10.3847/1538-4357/acf314)
- White, S. D. M., & Rees, M. J. 1978, *MNRAS*, 183, 341, doi: [10.1093/mnras/183.3.341](https://doi.org/10.1093/mnras/183.3.341)
- Zhao, H. 1996, *MNRAS*, 278, 488, doi: [10.1093/mnras/278.2.488](https://doi.org/10.1093/mnras/278.2.488)